TU Delft

Delft University of Technology

Document Version
Final published version

Licence
CC BY

Citation (APA)
van den Brink, M., Stam, M., Claassens, N. J., & Danelon, C. (2026). Image-based phenotypic sorting of synthetic cells. *Science Advances*, *12*(23), Article eaed0860. https://doi.org/10.1126/sciadv.aed0860

Important note
To cite this publication, please use the final published version (if applicable).
Please check the document version above.

Copyright
In case the licence states “Dutch Copyright Act (Article 25fa)”, this publication was made available Green Open Access via the TU Delft Institutional Repository pursuant to Dutch Copyright Act (Article 25fa, the Taverne amendment). This provision does not affect copyright ownership.
Unless copyright is transferred by contract or statute, it remains with the copyright holder.

Sharing and reuse
Other than for strictly personal use, it is not permitted to download, forward or distribute the text or part of it, without the consent of the author(s) and/or copyright holder(s), unless the work is under an open content license such as Creative Commons.

Takedown policy
Please contact us and provide details if you believe this document breaches copyrights.
We will remove access to the work immediately and investigate your claim.

This work is downloaded from Delft University of Technology.

Check for updates

SYNTHETIC BIOLOGY

Image-based phenotypic sorting of synthetic cells

Marijn van den Brink[1], Marlena Stam[1], Nico J. Claassens[2], Christophe Danelon[1,3]*

Understanding the relationships between genotype and phenotype is key to many areas of biological research and to the development of synthetic cells. We describe an image-based screening and sorting workflow that explores the phenotypes of gene-expressing vesicles within nonclonal populations and selects the desired variants. Using automated confocal microscopy and real-time, neural network–assisted image analysis, we demonstrate that liposomes can be selected for fluorescence intensity, protein localization, membrane morphology, and dynamic behaviors, and their phenotype can be linked to genetic content. This approach could substantially accelerate the evolution of cellular functions in a minimal synthetic context.

Copyright © 2026 The Authors, some rights reserved; exclusive licensee American Association for the Advancement of Science. No claim to original U.S. Government Works. Distributed under a Creative Commons Attribution License 4.0 (CC BY).

INTRODUCTION

Modular reconstitution of basic cellular functions in liposomes has laid the groundwork for building up an entire synthetic cell. For instance, DNA replication (*1*), transcription-translation (*2*–*4*), phospholipid synthesis (*5*–*8*), and membrane remodeling (*9*–*14*) have already been reconstituted in liposomes. The functional states of the engineered liposomes are commonly assessed by fluorescence microscopy techniques, including imaging flow cytometry (IFC) (*15*). Image-based methods allow for the exploration of a large observation space, defined as the set of features making up a liposome's phenotype. Therefore, vesicles exhibiting complex phenotypes—e.g., dynamic behaviors, spatial organizations, and membrane morphologies—can be identified, expanding the range of target functions toward which liposomes can be engineered, ultimately accessing a high degree of "aliveness."

When the liposome's phenotype is directed by a gene expression program, methods of in vitro evolution can be applied to accelerate the search for a desired function (*16*, *17*). Here, diversity is created by producing genetic variants directly inside liposomes (*18*) or externally before random encapsulation (*19*), leading to heterogenous nonclonal populations of liposomes exhibiting various, potentially distinct phenotypes. A major challenge resides in linking the specific phenotypes to their respective genotypes for sequence-function mapping. Pooled genetic screening of library variants in liposomes and isolation of the best-performing ones can be achieved by fluorescence-activated cell sorting (FACS) (*19*–*25*). However, phenotypic interrogation here relies on unidimensional parameters, which restricts selection to simple properties.

Technological advances in image-based screening and sorting of cells are revolutionizing our understanding of genotype-to-phenotype relationships with great implications in single-cell omics and clinical research (*26*). High-throughput image-activated cell sorters make sort decisions within micro- to milliseconds by real-time image analysis using predefined image parameters (*27*, *28*) and/or more powerful machine learning strategies (*29*) to classify complex phenotypes. However, drawbacks of these sorters are the low equipment accessibility, the limited spatial resolution, the limited number of fluorescence imaging channels, the inability to acquire time-lapse images or images in three-dimensional (3D) (at multiple *z* planes), or the possible impact of the flow on some phenotypic traits (*30*). Improved spatial resolution is obtained with IFC, but this technology lacks the ability to sort (*31*). An alternative method that offers improved spatial and temporal resolution is the two-step combination of microscopy and FACS. Microscopy images are analyzed in real time, whereafter the cells of interest are optically tagged for sorting by FACS. While this technique has been established for the analysis of mammalian and yeast cells (*32*–*38*), its potential in the research field of synthetic cells remains unexplored.

In this study, we describe a confocal microscopy–based method that assesses the phenotypes of gene-expressing liposomes and marks variants that exhibit the desired properties through selective photoactivation. Photoactivated liposomes are then isolated by FACS, and the enrichment of the functional variants is determined by quantitative polymerase chain reaction (qPCR) or DNA sequencing. High-resolution image acquisition, analysis, and photoactivation are fully automated using trained neural networks and predefined parameters (e.g., intensity, size, and circularity) for liposome classification. This approach allowed us to isolate liposomes with specific spatial and temporal features—including protein localization, membrane morphology, and dynamic behaviors—from large populations of hundreds of thousands of liposomes per experiment. Our work thereby establishes microscopy-based phenotypic selection of gene-expressing liposomes as a core technology for the construction of synthetic cells using a system's level evolutionary approach.

RESULTS

Establishing image-based liposome sorting

We aim to sort liposomes based on the visual phenotypes that arise from the expression of a library of different DNA variants. Synthesis of proteins that direct the phenotypic states is established directly in liposomes by the coencapsulation of DNA and a cell-free transcription-translation system (PURE system) (Fig. 1) (*39*). We used a laser-scanning confocal fluorescence microscope with a high numerical aperture objective to screen 50 to 150 liposomes per field of view (FOV), enabling precise examination of vesicle morphologies and subcellular features. The liposomes also encapsulate purified PAmCherry2, a photoactivatable mCherry, which marks individual liposomes for sorting when its fluorescence is activated by point stimulation with 405-nm light. Automated image acquisition, multimodal image analysis, and stimulation of targeted liposomes iterate over each FOV, allowing for the screening of hundreds of thousands

[1]Department of Bionanoscience, Kavli Institute of Nanoscience, Delft University of Technology, 2629 HZ Delft, Netherlands. [2]Laboratory of Microbiology, Wageningen University, Stippeneng 4, 6708 WE Wageningen, Netherlands. [3]Toulouse Biotechnology Institute (TBI), Université de Toulouse, CNRS, INRAE, INSA, 31077 Toulouse, France.
*Corresponding author. Email: danelon@insa-toulouse.fr

Downloaded from https://www.science.org at Delft University on June 17, 2026

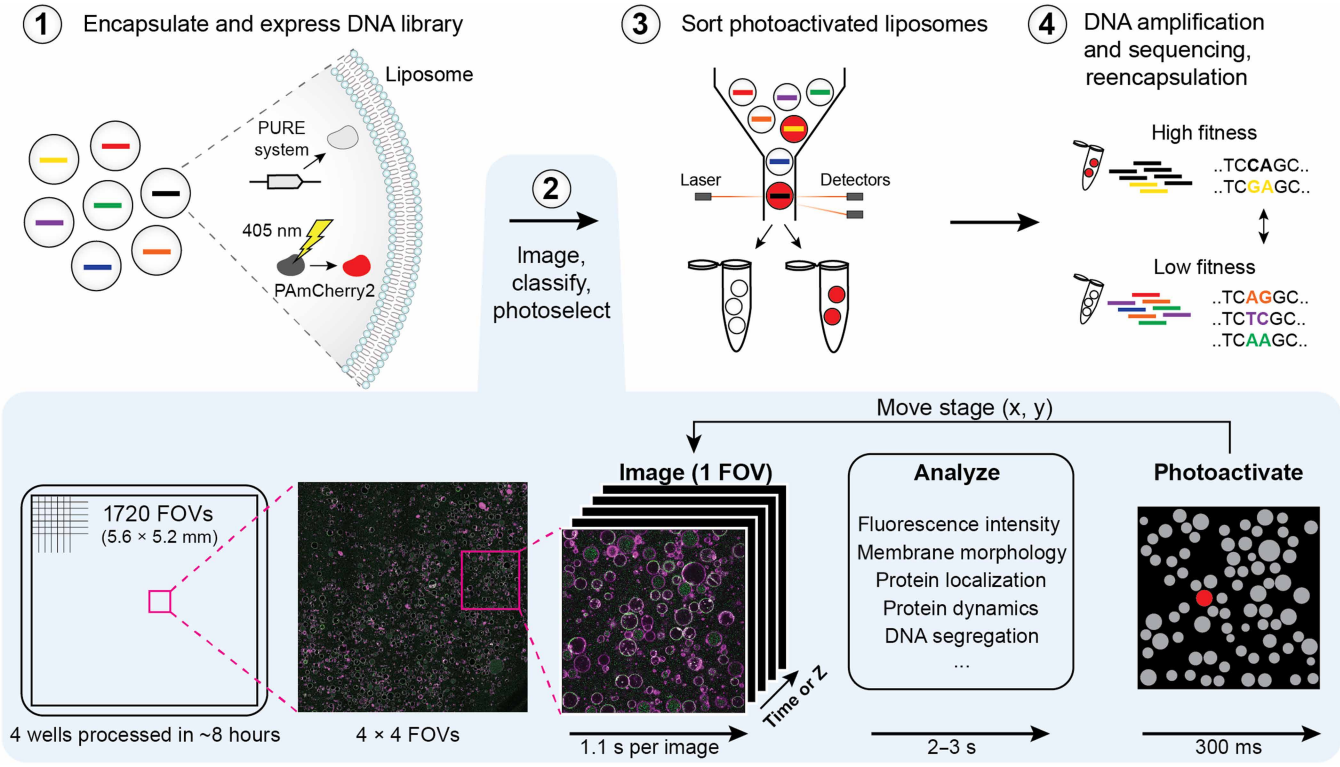


Fig. 1. Schematic workflow of image-based liposome sorting. Liposomes encapsulate a DNA library alongside PURE system and purified PAmCherry2. Automated imaging, real-time analysis, and point stimulation by 405-nm light to photoactivate PAmCherry2 in liposomes with a desired visual phenotype are iterated for each FOV. The duration of each step is indicated. The photoactivated liposomes (in red on the right-most picture) are then sorted by FACS, and DNA is recovered for analysis or re-encapsulation. The microscopy images were acquired in an experiment described in Fig. 4C and reused here as representative examples.

of liposomes per experiment of ~8 hours. Next, the liposomes with photoactivated PAmCherry2 are isolated using FACS, and the sorted DNA variants are analyzed by qPCR or PCR-amplified for DNA sequencing. The recovered variants could also be subjected to another round of diversification, reencapsulation, and sorting.

First, we verified that coencapsulation of 20 μM purified PAmCherry2 was compatible with the expression of a DNA template encoding yellow fluorescent protein (YFP) (Fig. 2A). Point stimulation (405-nm light at 84-μW laser power for 300 ms) of single liposomes located in the center *xy* coordinate of the FOV led to an increase in PAmCherry2 intensity in the entire lumen. Imaging at different *z* planes confirmed that, while a variety of liposome sizes was present (from 2 up to 20 μm in diameter), most of the vesicles were captured in a single *z* plane ~2 to 3 μm above the glass surface (Fig. 2A). This is especially important for preventing off-target photoactivation in liposomes located within the cone-shaped illumination volume above and below the focal point. After photoactivating 29 liposomes with expressed YFP, all liposomes showed an increase in PAmCherry2 fluorescence intensity (Fig. 2A).

Next, we examined the accuracy of PAmCherry2 photoactivation for different laser powers (34, 84, or 167 μW). All target liposomes were successfully tagged for the three photoactivation conditions with no significant differences in the median intensity values (fig. S1A). We then measured the lumen intensities of all other liposomes within 15-μm *xy* distance to the point of stimulation and found activation precisions of 96% at 34 μW, 89% at 84 μW, and 86% at 167 μW (fig. S1A). Thus, 34-μW laser power is the preferred choice, enabling photoactivation of all target liposomes while limiting off-target activation. We also measured the movement of liposomes over a period of 10 s, a time sufficient for imaging, real-time analysis, and photoactivation. The displacement of the liposome center coordinate was 0.5 ± 0.3 μm ($n = 15$ liposomes), thus too small to cause off-target photoactivation.

We observed a positive correlation between the fluorescence intensities of YFP and activated PAmCherry2 (fig. S1B). Specifically, upon photostimulation of liposomes that did not show YFP expression, these liposomes did also not exhibit post-activation PAmCherry2 signal. This result suggests that the encapsulation efficiency of different macromolecules in the swelling solution may be correlated. Furthermore, the YFP signal did not bleach upon photostimulation (fig. S1C), and the activated PAmCherry2 was stable for at least 21 hours, giving enough time to sort the tagged liposomes by FACS (fig. S1, D and E).

Image-based enrichment of YFP-expressing vesicles

To assess the performance of the imaged-based selection pipeline, we quantified the precision and sensitivity for sorting YFP-expressing liposomes starting from a two-gene mock library. A mixed population of liposomes containing PAmCherry2, PURE system, and either a *YFP* gene or a control gene (1:39 volume ratio) was processed (Fig. 2, B to D). The YFP-expressing liposomes were identified in real time using basic analysis parameters including intensity thresholding, object size, and circularity and were photoactivated. Per replicate experiment, we screened liposomes in 2000 to 5000 FOVs (31

Downloaded from https://www.science.org at Delft University on June 17, 2026

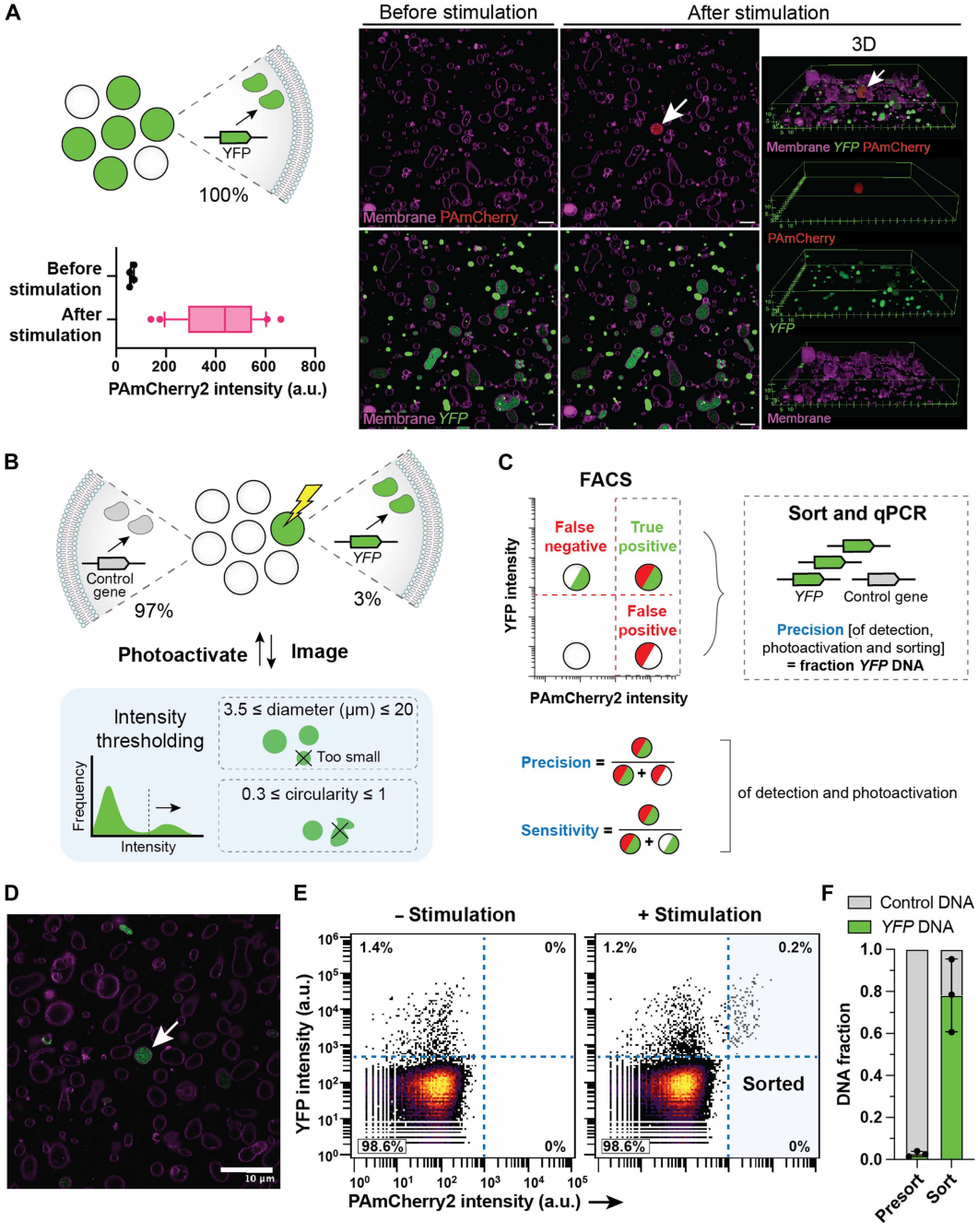


Fig. 2. Image-based sorting of YFP-expressing liposomes. (**A**) Photoactivation of PAmCherry2 in YFP-expressing liposomes. Liposomes contained 5 nM *YFP* DNA template and 20 μM purified PAmCherry2. Stimulation was performed in the center of the FOV using 84-μW laser power for 300 ms. The PAmCherry2 fluorescence intensity was measured 10 s after stimulation. Graph displays $n = 29$ liposomes. Scale bars, 10 μm. (**B**) Image-based sorting of YFP-expressing liposomes from a two-gene mock library prepared by mixing two populations of liposomes at a 1:39 volume ratio, each containing an equal amount of linear DNA template, either *YFP* or *btubB* (control gene). Automated image analysis was performed using intensity thresholding on the YFP signal. (**C**) Precision and sensitivity of the method were assessed using FACS and qPCR analysis of the *YFP* and control DNA in the sorted liposomes. (**D**) Example microscopy image of the mock library. Green, YFP; magenta, Cy5-conjugated lipids. Scale bar, 10 μm. Arrow indicates liposome selected for photostimulation [300 ms at 34-μW (replicates 1 and 2) or 84-μW (replicate 3) laser power]. (**E**) Flow cytometry measurements of liposome populations without (28,898 events) or with (54,490 events) stimulation. (**F**) Fractions of *YFP* and control DNA in the sorted and presort liposome samples. $n = 3$ biological replicates (distinct mixed liposome populations). a.u., arbitrary units.

Downloaded from https://www.science.org at Delft University on June 17, 2026

to 77 mm^2) and photoactivated ~800 to 7200 liposomes (table S1). Stimulated and nonstimulated samples were analyzed by flow cytometry (Fig. 2E, fig. S2, and table S2). Approximately 1 to 2% of the liposomes were expressing YFP. This percentage is in agreement with the ratio at which the liposome populations were mixed (1:39) and the percentage of YFP-expressing liposomes in the initial population prior mixing with the control population (40 to 80%). While the nonstimulated sample only showed liposomes with a low PAmCherry2 signal, the stimulated sample yielded 0.3 ± 0.1% of the liposomes with a high PAmCherry2 signal ($n = 3$ biological repeats). By processing the events in the four quadrants as indicated in Fig. 2C, we found that the YFP-expressing liposomes were detected and photoactivated with a precision of 100% (using laser power 34 μW) (Fig. 2E). Two replicate experiments with laser power 84 μW and where stimulation was not restricted to center of FOV resulted in a precision of 47 ± 8% (fig. S2). In addition, 15.3 ± 0.2% ($n = 3$) of the YFP-expressing liposomes were photoactivated. This value defines the sensitivity and is specific to this experiment. It could be improved by increasing the fraction of the sample that was screened (here, only 50 to 80% of the chamber bottom surface was imaged) and making the detection less stringent on liposome size and circularity. Ten to 20% of the photoactivated liposomes were detected by FACS and sorted, corresponding to 150 to 900 liposomes (table S1). Last, the enrichment of the *YFP* gene over the control gene was quantified by qPCR (Fig. 2F and table S3). The percentage of *YFP* amount increased from 3 ± 1% to 78 ± 17%, corresponding to a 39 ± 28 fold enrichment ($n = 3$).

We further investigated the possible contribution of off-target stimulation to the presence of the control gene in the sorted fraction by directly sorting YFP-expressing liposomes from the mixed population by FACS, i.e., without imaging. Here, we obtained a percentage of *YFP* in the DNA pool of 81 ± 6% ($n = 4$) after sorting (fig. S3 and tables S4 to S6) (to be compared to 78% with the image-based workflow), indicating that photostimulation did not significantly affect the sorting precision.

Real-time, neural network–assisted detection of liposomes and spatial protein organization

Deep learning models have become state of the art for image analysis thanks to their high prediction speed, robustness to biological variability, noisy data and varying imaging conditions, and reduced bias from manual parameter tuning (*40*, *41*). Therefore, the single-stage object detector You Only Look Once (YOLO) (*42*–*44*) was chosen and used to identify liposomes in real time based on their membrane morphology and the spatial organization of fluorescent proteins. As a proof of principle, we applied YOLO to detect proteins of the Min system, a regulator of bacterial cytokinesis and a candidate for the reconstitution of division processes in synthetic cells (*10*, *45*). This protein system displays spatiotemporal organization when encapsulated in liposomes, providing an ideal study case for selection based on dynamic behaviors. We expressed the membrane binding protein MinD from a *minD* DNA template and added the purified enhanced green fluorescent protein (eGFP)–MinC fusion protein as a reporter of the presence of active MinD (Fig. 3A). The localization of eGFP-MinC in the lumen would indicate the absence of MinD, while its localization at the membrane would reveal the functional expression of MinD.

As training data, we used 700 images of liposomes containing both the lipid membrane and eGFP-MinC channels (Fig. 3B). The dataset originated from multiple liposome samples (biological replicates) to increase the model's robustness to variation in sample preparation and imaging conditions. Each image displayed many liposomes with various phenotypes: no eGFP-MinC signal, eGFP-MinC on the membrane or/and in the lumen, unilamellar or multilamellar vesicles, circular liposomes or structures with other shapes, and a wide distribution of sizes. We annotated 688 objects in one class, aiming for unilamellar, circular liposomes of 3 to 15 μm in diameter with eGFP-MinC on the membrane. Using 80% of the labeling dataset, we trained YOLOv3-tiny (*43*) with pretrained weights and both YOLOv3-tiny and YOLOv7-tiny (*44*) with and without pretrained weights (fig. S4A). We tested the two models using the remaining 20% images and found that the best-performing model was YOLOv7-tiny with a precision of 82% and recall of 82% at a confidence threshold of 0.8 (Fig. 3C). Communication between the image acquisition software and the trained YOLOv7-tiny model was established for real-time image analysis and photoactivation.

Two populations of liposomes containing PAmCherry2, PURE system, purified eGFP-MinC, and either the *minD* gene or a control gene were mixed in a 1:9 ($n = 1$) or 1:39 ($n = 2$) ratio (*minD*/control gene) (Fig. 3A). Liposomes exhibiting eGFP-MinC signal at the membrane were photostimulated to select vesicles containing *minD* (Fig. 3D and table S7). Photoactivated liposomes representing 0.03 to 0.94% of the total population were sorted by FACS (Fig. 3E, fig. S5, and table S8), and the fractions of gene variants were quantified by qPCR in the presort and sorted liposome samples. The percentage of *minD* increased from 7 ± 7% in the presort sample to 81 ± 18% after sorting, corresponding to a 19 ± 12 fold enrichment ($n = 3$ biological repeats) (Fig. 3F and table S9). Because neural network analysis can be applied to identify images with rich spatial and morphological information, these results show the potential of our method for the selection of synthetic cells with complex phenotypes from heterogeneous samples.

Video-based photoactivation of liposomes displaying dynamic protein oscillations

As flow-based image-activated sorters can only detect static features, we sought to exploit our method to photoactivate liposomes based on dynamic processes. In *Escherichia coli*, the Min system undergoes oscillatory behaviors that aid in positioning the division site (*46*). In liposomes, the coexpression of MinD and MinE leads to different types of dynamic behavior, including pulsing, circling, and pole-to-pole oscillations with periods typically ranging from 15 to 45 s (Fig. 4A) (*10*). Liposomes can also exhibit an uncategorized or halted dynamic mode, and modes can switch from one to another or change directionality, leading to a large variability in dynamic and static phenotypes within one liposome sample. Consequently, time-lapse microscopy is required to assess whether a liposome exhibits a dynamic or static organization of Min proteins. To detect the temporal behaviors of the Min proteins in real time, the liposomes were imaged with 12-s intervals over a period of 48 seconds. We trained YOLOv7-tiny to detect two classes: Class 1 consists of liposomes with eGFP-MinC not located on the membrane, while class 2 consists of liposomes with eGFP-MinC (partly) located on the membrane (Fig. 4B). The model was trained on 80% of the images and tested using the separate 20% of the dataset, yielding a precision of 83% and recall of 86% at a confidence threshold of 0.9 (fig. S4B). Hereafter, we

Downloaded from https://www.science.org at Delft University on June 17, 2026

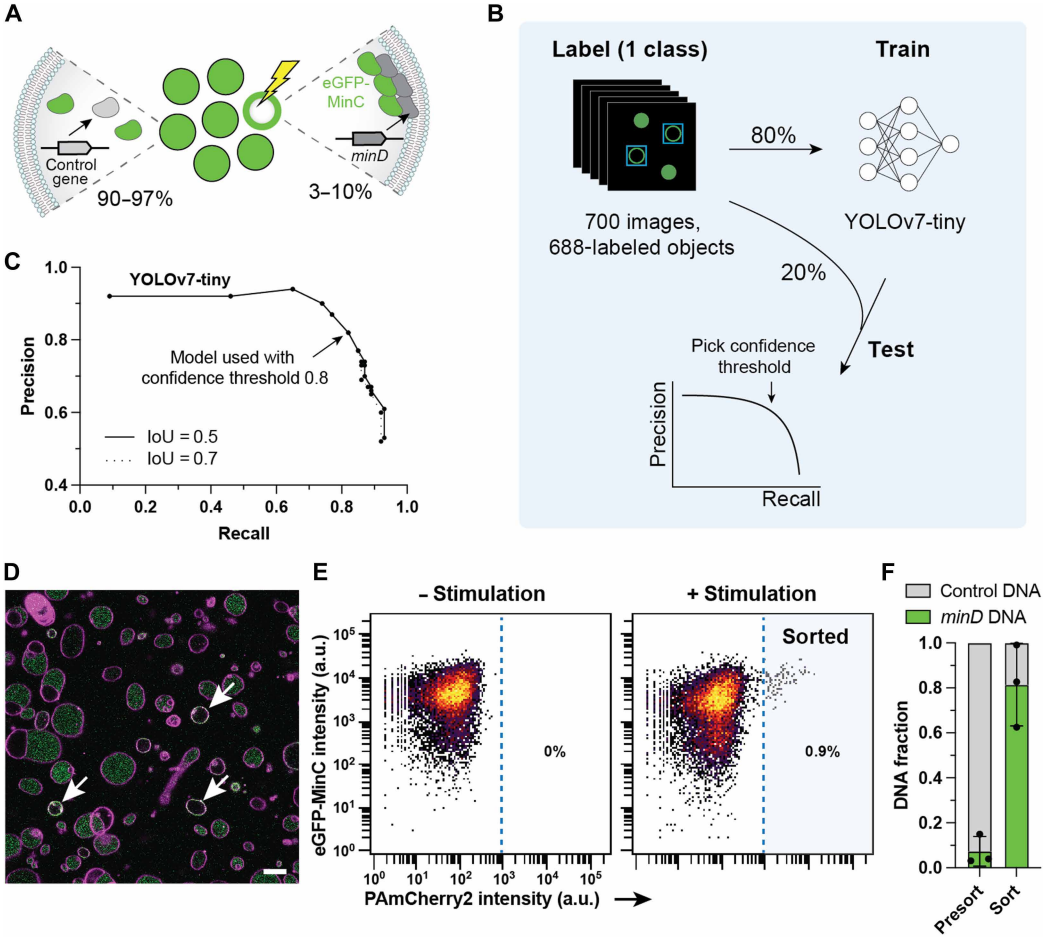


Fig. 3. Image-assisted sorting of membrane-localized MinD using deep learning. (**A**) A mock DNA library was prepared by mixing two populations of liposomes (1:9 or 1:39 volume ratio) expressing either *minD* or *btubB* (control gene) and containing 500 nM purified eGFP-MinC. When MinD is expressed, it binds to the membrane and recruits eGFP-MinC. (**B**) Labeling, training, and testing of YOLOv7-tiny using images displaying the membrane reporter dye Cy5 and GFP signals. (**C**) Performance of the trained YOLOv7-tiny model. IoU, Intersection over Union. (**D**) Example microscopy image of the mock library. Green, eGFP-MinC; magenta, Cy5-conjugated lipids. Scale bar, 10 μm. Automated image analysis was performed by the trained YOLOv7-tiny model. Arrows indicate liposomes classified for photostimulation during 300 ms at 34-μW or 84-μW laser power (table S7). (**E**) Flow cytometry measurements of liposome populations without (10,365 events) or with (10,262 events) stimulation. Between 170 and 900 liposomes were sorted per replicate. (**F**) Fractions of *minD* and control DNA in the sorted and presort liposome samples. $n = 3$ biological replicates.

retrained a model on the complete labeled dataset (700 to 900 objects per class).

Detected liposomes were tracked across multiple time frames using a nearest-neighbor search (Fig. 4B). While most liposomes remained stationary during the measurements, a few moved substantially in *xy* direction, increasing the likelihood of being misidentified as a different liposome. Therefore, we applied a 5-μm maximum displacement threshold relative to the position in the first frame. Then, each class for a given liposome was compared over the consecutive time frames. The change from one class to the other reveals a dynamic event and these liposomes were photoactivated. In 8 hours, we screened ~40,000 liposomes and stimulated one liposome in every 2 FOVs (~0.5% of all liposomes) (Fig. 4C and table S10). Manual labeling of liposomes showing both the presence and absence of membrane-localized eGFP-MinC across different time frames resulted in a precision of 76 ± 10% and a sensitivity of 44 ± 5% ($n = 3$ biological repeats), validating video-based classification of liposomes (Fig. 4D).

Selection of best-performing membrane binders from a library of *minD* variants

At last, we showed that image-based screening and sorting can be successfully coupled to the recovery and sequencing of DNA from the sorted liposomes. We sought to find the best-performing variants within a *minD* library harboring mutations in the hydrophobic patch of the membrane targeting sequence (MTS) (*47*), most likely conferring different abilities to bind to the liposome membrane. Nine DNA variants were separately encapsulated and expressed in liposomes, whereafter the clonal liposome populations were mixed and subjected to the image-based selection pipeline to sort the liposomes with membrane-localized eGFP-MinC (Fig. 5B, fig. S6, and tables S11 and S12). The DNA was recovered by PCR from 88 up to

Downloaded from https://www.science.org at Delft University on June 17, 2026

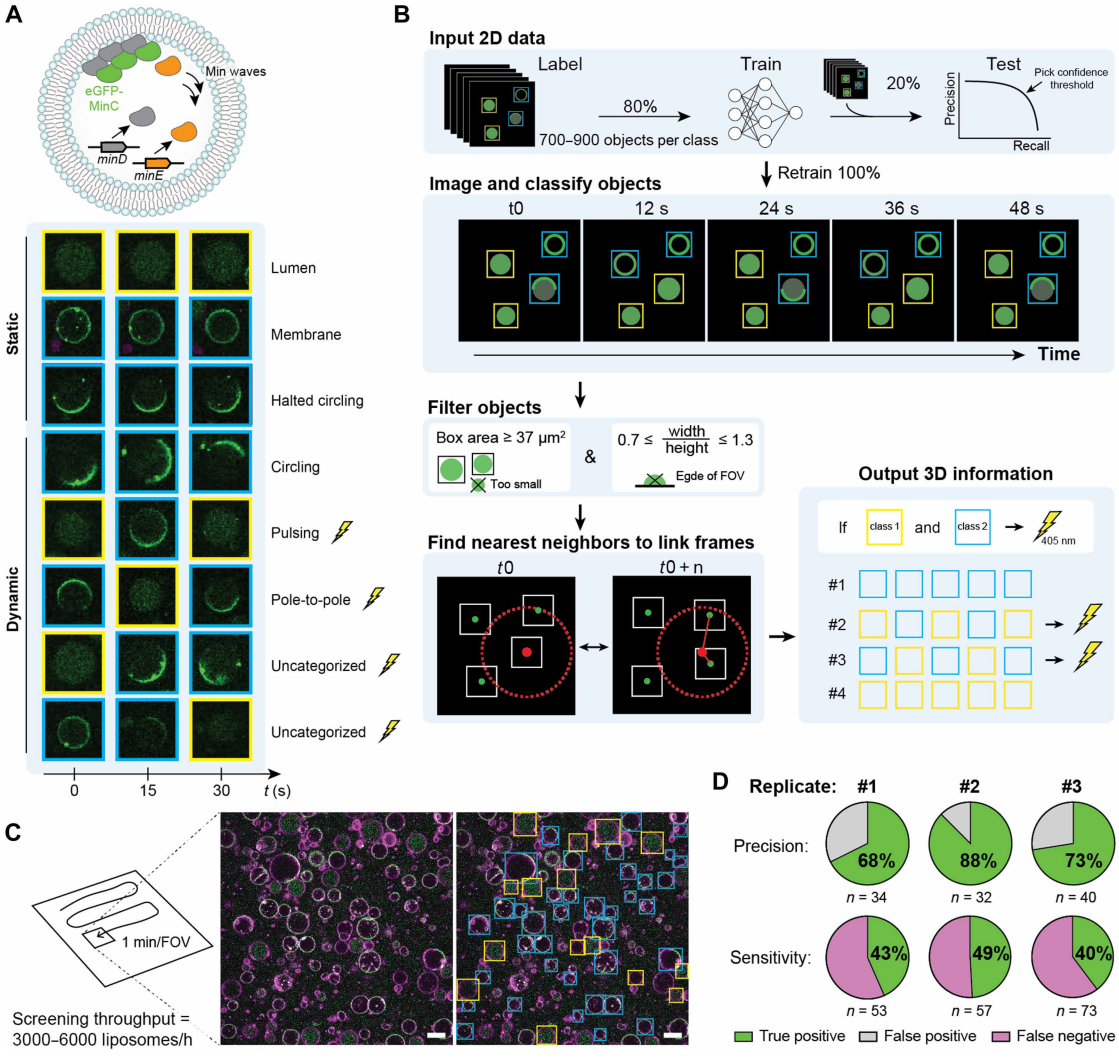


Fig. 4. Real-time detection and tagging of liposomes with dynamic Min oscillations. (**A**) Min oscillations driven by the coexpression of MinD and MinE were visualized using purified eGFP-MinC. Representative images of eight liposomes exhibiting static or dynamic behaviors. Only liposomes with dynamic patterns were photoactivated. (**B**) Automated image analysis pipeline. Liposomes were detected using a YOLOv7-tiny model, trained on 2D data using two classes (indicated with blue and yellow bounding boxes). To assure accurate liposome tracking across time frames, small liposomes (diameter < 6 µm), which tend to move in and out of focus more than larger liposomes, and liposomes with aspect ratio below 0.7 and above 1.3 were excluded. Linking multiple time frames through a nearest neighbor search enabled the discrimination of static versus dynamic behaviors. (**C**) Automated acquisition of liposome images and real-time identification of static versus dynamic self-organization of Min proteins. One example microscopy image is presented twice: without (left) and with (right) annotation of the detected liposomes. Blue boxes indicate detected liposomes, where Min proteins localize at the membrane, and yellow boxes indicate liposomes where the fluorescent proteins did not localize to the membrane. Scale bars, 10 µm. (**D**) Performance of the classification pipeline. Precision and sensitivity were calculated relative to the ground truth, which entailed manual classification of the liposomes in the videos. $n = 3$ biological replicates. Stimulation time was 300 ms, and laser power was 34 µW. The YOLOv7-tiny model from replicate 1 was retrained with nine additional images to strengthen the model (fig. S4B). For replicates 1 and 2, a population of liposomes expressing MinD and MinE was mixed 1:1 with liposomes expressing MinD and a control protein (BtubB). For replicate 3, only liposomes expressing MinD and MinE were used.

704 sorted liposomes per biological replicate (Fig. 5C and fig. S7C), and the fraction of each variant before and after sorting was quantified by Nanopore sequencing (Fig. 5D). From the nine variants present in the input library, only two were found in the sorted pool: Var1 (the wild type) and Var7 (amino acids: FL > LH). The encapsulation and expression of the individual variants confirmed that Var1 and Var7 encode a membrane-binding MinD, while the other mutants could not (Fig. 5E and fig. S7, A and B). These results are in agreement with a previous study that showed that the substitution of hydrophobic amino acids to charged amino acids in the MTS caused defective binding of MinD to the membrane in *E. coli* (*47*). Together, these findings demonstrate the feasibility to isolate and genotype active gene variants from a library using image-based liposome phenotyping.

DISCUSSION

We describe a confocal microscopy–based method that explores the phenotypes of gene-expressing liposomes within large populations and sorts the desired variants using photo-tagging followed by

Downloaded from https://www.science.org at Delft University on June 17, 2026

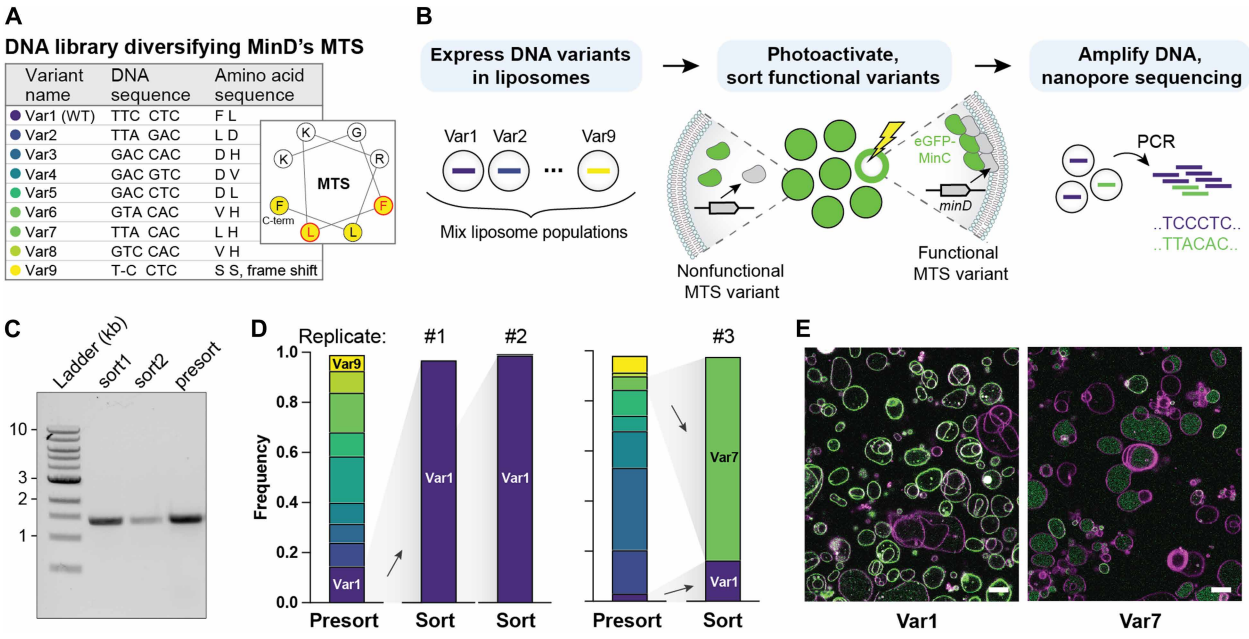


Fig. 5. Enrichment of active *minD* variants from a library. (**A**) Design of the library of MTSs in the gene *minD*. Mutations were introduced in two of the codons in the hydrophobic patch of the highly conserved MTS motif of MinD. (**B**) Image-based sorting of liposomes expressing MinD variants with different affinities to the membrane. Populations of clonal liposomes, each containing one library variant, were pooled and subjected to image-based selection. Mutations lead to differential localization of eGFP-MinC to the membrane (functional MTS) or to the lumen (nonfunctional MTS). DNA was amplified from the sorted liposomes by PCR and sequenced. Stimulation time was 300 ms, and laser power was 34 μW. (**C**) Gel electrophoresis with PCR-amplified *minD* (1398 bp) recovered from liposomes sorted by FACS. (**D**) Frequency of the DNA variants was quantified using Nanopore sequencing before and after liposome sorting. Two starting ratios of the nine DNA variants were prepared, from which, in total, three sorting replicates were performed. (**E**) Confocal microscopy images of the two enriched variants (Var1 and Var7) separately encapsulated and expressed in liposomes. These images are also presented in fig. S7A. Green, eGFP-MinC; magenta, Cy5-conjugated lipids. Scale bars, 10 μm. WT, wild type.

FACS. Our results offer a new promising way to accelerate the development of synthetic cells through in vitro evolution, whereby the system's fitness is assessed by visual screening. With this objective in view, we here discuss the current assets of the proposed technology compared to existing ones (see fig. S8 and data S1 for benchmarking analysis) and possible extensions that could enable the discovery of phenotypically complex synthetic cells from a large library of genetic and molecular variants.

Unlike traditional methods that enrich variants based on one-dimensional readouts in time and space, such as FACS (*19*–*25*), affinity-based selection (*17*, *48*), and self-selection through DNA replication (*18*), visual phenotyping allowed us to classify liposomes based on morphology and spatiotemporal protein organization. While photoselection-based methods similar to ours have been developed for biological cells (*32*–*38*), working with liposomal synthetic cells imposes several challenges: the small size (diameter < 10 μm), polydispersity and low phase-contrast of the vesicles, stochastic encapsulation of the photoactivatable probe, and positioning of the liposomes on a 2D surface. Because of these constraints, we chose confocal fluorescence imaging using a high numerical aperture (NA, 1.49, 100× oil immersion) objective to measure with a high spatial resolution. Despite the small size of the liposomes, the photoactivation of single vesicles was accurate and sensitive; all liposomes that displayed gene expression also exhibited higher PAmCherry2 fluorescence after stimulation (Fig. 2 and fig. S1).

In this work, we explored a combined set of liposome features including fluorescence intensity, protein colocalization to the membrane or lumen, and liposome morphology. We also introduced a temporal dimension by linking these phenotypes across time frames. By capturing 50 to 150 liposomes per FOV (128 μm by 128 μm), we screened up to 700,000 liposomes per experiment of ~8 hours (including photoactivation). We demonstrated successful recovery and sequencing of the DNA underlying the selected phenotypes for typical sorting fractions of 150 to 1000 liposomes, and we could even recover the DNA from as low as 88 sorted liposomes. We showcased the enrichment of the most active DNA variants from a library of nine variants (Fig. 5). The next step in image-based sorting of synthetic cells is enlarging the library size to hundreds or thousands of variants to make better use of the available screening capacity. This will require establishing a method for multiplexing liposome production, where many liposome samples can be prepared in parallel, for example, using laboratory automation. Alternatively, the DNA library could be encapsulated in a single liposome sample at a low DNA concentration (~1 copy per liposome), but this strategy demands an increase in the fraction of active liposomes to enable screening of large libraries, for instance, by coupling gene expression with clonal amplification (*49*). These approaches should go hand-in-hand with smart library design and active learning-assisted directed evolution to enable efficient screening of large genetic and molecular spaces by focusing experimental testing to a smaller subset containing the most informative variants (*50*, *51*).

In clonal liposome samples, only 40 to 80% of the liposomes show gene expression above the detected threshold (Fig. 2A and fig. S2). Nongenetic factors that may affect protein production include liposome size, membrane permeability to low–molecular weight compounds [e.g., nucleoside triphosphates (NTPs), amino acids, and

Downloaded from https://www.science.org at Delft University on June 17, 2026

energy substrates], and encapsulation efficiency of PURE system components (*52*). We assume that such a heterogeneity does not bias genotype enrichment because it similarly manifests for each DNA variant in the library, and phenotypic selection still hinges on vesicles encapsulating the best performing genetic variants. However, these effects raise the number of liposomes to be screened for efficient library coverage.

We typically photoactivated 1000 to 10,000 liposomes of which we sorted 100 to 1000 by FACS (tables S1, S7, and S11). The 10% recovery rate of photoactivated liposomes could limit the sorting efficiency when the phenotypes of interest are extremely rare. Given that not all liposomes within a clonal population are active (say 10% as a lower bound), our method can assess 200,000 DNA variants when screening 2 million liposomes, which takes ~24 hours microscope time. Considering a minimum of 1000 photoactivated liposomes, our method is currently most suited for DNA libraries with at least 1 in 200 beneficial DNA variants. The 10% recovery rate of photoactivated liposomes by FACS is somewhat lower than those reported for cells (26 to 54%) (*33*, *38*). The disruption of liposomes, incomplete harvesting during transfer from the imaging well to the FACS instrument, or the low scattered light intensity of the liposomes may explain this observation. Potential improvements include using the PAmCherry2 signal instead of the scattered light intensity to trigger event recording during FACS and designing microscopy chambers that would facilitate harvesting of the liposomes. Furthermore, the PAmCherry2 concentration could be increased, or an alternative photoactivatable protein or dye could be used.

While the screening throughput depends on the number of stimulated liposomes per FOV, it is on par with that of existing methods applied to biological cells (data S1). Yet, it is low compared to flow-based imaging sorters that can typically analyze samples at a speed of 10^2 to 10^3 events per second (*27*, *29*). Strategies to increase the throughput include (combinations of) shortening (i) the acquisition time by using a spinning-disk confocal microscope, (ii) the analysis time by processing multiple FOVs simultaneously or speeding up the communication between acquisition and analysis, and (iii) the stimulation time while increasing the 405-nm laser power. Noteworthy, ultrawide-FOV microscopes could markedly increase the throughput by imaging FOVs of ~5 to 42 mm^2 at millisecond temporal resolution (*36*, *37*, *53*). However, a better trade-off will have to be found for improving the spatial resolution (NA objective of 0.25 or 0.5) (*36*, *37*, *53*) as it is currently insufficient for the characterization of internal liposome structures. The same limitation of the spatial resolution also applies to the flow-based imaging sorters IACS2.0 (*29*) and BD FACSDiscover S8 (*27*, *28*).

High-content imaging, which captures multiple features of gene-expressing liposomes, enables multiobjective optimization that reflects the integrated activities of several biological processes. As the number of reconstituted biological modules increases, the liposome phenotypes become more complex, and the observation space becomes larger. Therefore, sorting multiple subpopulations would be very useful to obtain a more holistic view of the effects of genetic and molecular variations on the phenotype—beyond the best-performing variants only. This allows better identification of neutral and deleterious mutations and may provide deeper insights into mutational effects across different genetic or molecular backgrounds (*54*). Sorting multiple subpopulations might be achieved by varying the activation time or laser power and sort multiple phenotypes by FACS based on PAmCherry2 intensity thresholding (*32*, *34*). However, the overlap of PAmCherry2 intensity distributions at laser powers spanning 34 to 167 μW currently challenges multiway sorting of photoactivated liposomes. Adjusting both the laser power and stimulation time might generate distinct PAmCherry2 intensity profiles.

While in this work, liposomes were prepared via gentle hydration of lipid films dried on glass beads (*55*), the screening-sorting workflow could also be applied to gene-expressing giant liposomes formed via alternative protocols, such as water-in-oil droplet transfer across an oil-water interface (*3*, *56*) or droplet-based microfluidics (*57*). Furthermore, in addition to DNA sequencing, the sorted liposome fractions could be subjected to other analytical investigations to reveal a rich array of cellular properties and functions, which can be coupled to the fitness level and genotype of each subpopulation. Recent advances in single-cell omics could be applied to gene-expressing liposomes for mapping genotype and detailed molecular information, e.g., proteins, RNA transcripts, and metabolites (*32*, *36*, *58*, *59*).

Last, the current classification strategy relies on predefined metrics of physical parameters or on supervised machine learning with liposome images annotated by the user. This approach introduces potential human bias that narrows the exploration of phenotypic states. Unsupervised methods based on the structure of the data itself and lacking an explicit optimization target may increase robustness and expand the range of possible discoveries by revealing difficult-to-identify or hidden properties of the liposomes (*60*). Implementing unsupervised learning to our imaging-based pipeline would lay the foundation for open-ended evolution of synthetic cells (*16*).

MATERIALS AND METHODS

Reagents and plasmid DNA

Solutions were prepared using Milli-Q water with 18.2-MΩ resistivity (Merck Millipore). Reagents were purchased from Sigma-Aldrich unless indicated otherwise. Primers and plasmids are listed in tables S13 and S14, respectively. Plasmids G365 (pUC-*YFP*) and G437 (pUC-*minD*) were constructed as described earlier (*49*). G439 (pUC-*btubB*) was constructed as described earlier (*12*). G376 (pUC-*minE_opt*) was ordered from GenScript, as described earlier (*10*). The expression vector G595 (pET15b-*PAmCherry2*) was constructed by cloning of the *PAmCherry2.1* gene (*61*) (amplified with primers 1429 ChD and 1430 ChD) into the pET15b backbone (amplified with primers 1431 ChD and 1432 ChD) using Gibson Assembly. The expression vector G577 (pET15b-mEos2) was constructed by cloning of the *mEos2* gene (amplified from G571 with primers 1355 ChD and 1356 ChD) into the pET15b backbone (amplified with 1353 ChD and 1354 ChD) using Gibson Assembly.

Protein purification

eGFP-MinC was purified as described in published protocols (*62*). To synthesize PAmCherry2 and mEos2, 10 ml of overnight culture of *E. coli* BL21 (DE3) (New England Biolabs) carrying G595 (PAmCherry2) or G577 (mEos2) was diluted 1:100 in Lysogeny Broth (LB) medium containing ampicillin (50 μg ml^{-1}). The diluted culture was grown in a shaking incubator at 37°C until the optical density at 600 reached 0.4 to 0.6. Gene expression, under control of the T7-LacO promotor and in frame with an N-terminal His-tag, was

Downloaded from https://www.science.org at Delft University on June 17, 2026

induced by addition of 0.25 mM (PAmCherry2) or 1 mM (mEos2) isopropyl-β-D-thiogalactopyranoside. The cells were incubated overnight at 16°C in a shaking incubator (PAmCherry2) or at 26°C for 4 hours (mEos2). The cells from 1 liter of culture were pelleted by centrifugation and resuspended in 10 ml of lysis buffer [50 mM Hepes-KOH (pH 7.5), 500 mM NaCl, and 10% glycerol]. The cells were sonicated in an ice bath six times 20 to 30 s with an interval of 1 min and an amplitude of 40%. After centrifugation at 16,000*g* for 15 min at 4°C, the cell-free extract (supernatant) was harvested. A 10 mM imidazole and SetIII protease inhibitor (EDTA free, 1:1000 dilution; Calbiochem) were added. The cell-free extract was mixed with a HisPure Ni-NTA resin (Thermo Fisher Scientific), priorly equilibrated with lysis buffer, and incubated at 4°C for 2 hours while tumbling. The unbound fraction was removed by spinning the resin at 750*g* for 2 min. The resin with bound protein was washed twice with 20 equivalents (volume) of wash buffer [50 mM Hepes-KOH (pH 7.5), 500 mM NaCl, 50 mM (PAmCherry2) or 40 mM (mEos2) imidazole, and 10% glycerol]. The protein was eluted with 6 ml of elution buffer [50 mM Hepes-KOH (pH 7.5), 500 mM NaCl, 500 mM imidazole, and 10% glycerol]. The fluorescent fractions (for mEos2) were pooled together and buffer-exchanged with storage buffer [50 mM Hepes-KOH (pH 7.5), 50 mM (PAmCherry2) or 100 mM (mEos2) NaCl, and 10% glycerol] using a 10 kDa MWCO Amicon Ultra-15 centrifugal filter unit (Merck). Protein concentration was determined with a Bradford assay.

Preparation of linear DNA templates for encapsulation in liposomes

Linear DNA templates for in-liposome expression were amplified by PCR from plasmids G365 (*YFP*), G439 (*btubB*), G437 (*minD*), and G376 (*minE*) with primers 757 ChD and 709 ChD annealing to the T7 promoter and T7 terminator, respectively. The PCR reactions were set up at 50-μl volume and contained 200 μM deoxynucleotide triphosphates (dNTPs), 500 nM each primer, plasmid DNA (200 pg μl^{-1}), and 1 U of Phusion High-Fidelity DNA Polymerase (Thermo Fisher Scientific) in 1× Phusion HF Buffer. The thermocycling reaction was performed as follows: 98°C for 30 s, (98°C for 10 s, 56°C for 20 s, and 72°C for 30 s) × 30, and 72°C for 10 min. The amplicons were purified directly or by gel extraction using the QIAquick PCR & Gel Cleanup Kit (QIAGEN). The DNA concentration was measured with the Qubit dsDNA High Sensitivity Assay Kit and the Qubit 4 Fluorometer (Invitrogen).

Synthesis of *minD* plasmid library and isolation of single variants

A 32-variant *minD* plasmid library (G598) with mutations in the MTS of MinD was synthesized by full-plasmid amplification of plasmid G437 (pUC19-*minD*) with a mutagenic primer set and subsequent recircularization using the protocol adapted from Galka *et al.* (*63*). PCR amplification was performed with primers 1445 ChD and 1448 ChD, of which the latter contains degeneracy at the MTS. The PCR reaction was set up at 20-μl volume and contained 400 μM dNTPs, 300 nM each primer, plasmid DNA (350 pg μl^{-1}), and 0.4 U of KOD Xtreme Hot Start DNA Polymerase in 1× KOD Xtreme PCR Buffer and 5% dimethyl sulfoxide. A touchdown thermocycling reaction was performed as follows: 94°C for 2 min, (98°C for 10 s, 74°C for 4.2 min) × 4, (98°C for 10 s, 72°C for 4.2 min) × 4, (98°C for 10 s, 70°C for 4.2 min) × 4, (98°C for 10 s, 60°C for 20 s, 70°C for 4.2 min) × 12, and 70°C for 5 min.

Because the two primers are (partly) complementary, the two ends of the amplicon were identical, enabling recircularization by mixing 18 μl of the PCR reaction with 54 μl of a Gibson reaction mix containing 1.3× ISO buffer [0.5 M of tris-HCl (pH 7.5); 50 mM $MgCl_2$; 4 mM dNTP mix; 50 mM DTT; polyethylene glycol, molecular weight 8000 (PEG-8000) (0.25 g ml^{-1}); and 5 mM nicotinamide adenine dinucleotide], T5 exonuclease (0.053 U μl^{-1}; Epicentre), Phusion High-Fidelity DNA polymerase (0.0033 U μl^{-1}; Thermo Fisher Scientific), Taq DNA ligase (5.3 U μl^{-1}; NEB), and Dpn I endonuclease (50 U ml^{-1}; NEB). The reaction was incubated in a thermocycler at 50°C for 2 hours. The full reaction was loaded onto a 0.7% agarose gel, and the band corresponding to the circularized amplicon was purified by gel excision and further purified using the QIAquick PCR & Gel Cleanup Kit (QIAGEN).

Next, 50 μl of competent *E. coli* K-12 DH5α cells were transformed with 3 ng of purified plasmid using heat shock. Single colonies were picked from ampicillin-supplemented LB agar plates and grown overnight in ampicillin-supplemented (50 μg ml^{-1}) LB medium. The plasmids were isolated with the PureYield Plasmid Miniprep System (Promega), and their sequences were analyzed by Sanger sequencing (Macrogen Europe, Netherlands) using primer 709 ChD.

Liposome preparation

The swelling solutions (10 μl) were prepared on ice by mixing 5 μl of PURE*frex* 2.0 Solution I, 0.5 μl of solution II, 1 μl of solution III, SUPERase·In RNase Inhibitor (0.75 U μl^{-1}; Ambion), 20 μM purified PAmCherry2, and 5 nM linear DNA template (unless indicated otherwise) in a 1.5-ml Eppendorf tube. When expressing proteins from the Min system, the solution was supplemented with 0.5 μM purified eGFP-MinC, 0.5 μl of DnaK Mix (GeneFrontier), and 2.5 mM adenosine 5′-triphosphate (ATP). The DNA concentration was adjusted to 6 nM *minD* and 3.8 nM *minE* when both proteins were coexpressed. Next, 5 to 6 mg of lipid-coated glass beads were added to the swelling solutions. The lipid-coated beads were prepared as described earlier (*52*) with minor modifications. The glass beads (0.6 g) were coated with 50 mol % dioleoylphosphatidylcholine, 36 mol % dioleoylphosphatidylethanolamine (DOPE), 12 mol % dioleoylphosphatidylglycerol, 2 mol % 18:1 cardiolipin, 0.05 mass % DOPE-Cy5, and 1 mass % DSPE-PEG(2000)-biotin with a total mass of lipids of 2 mg. The mixture containing PURE system and lipids was gently rotated at 4°C for 1 hour to allow for liposome swelling. Four freeze-thaw cycles were applied by dipping the samples in liquid nitrogen for 10 s, followed by thawing on ice.

In-liposome gene expression

For liposome samples containing *YFP*, *btubB*, or *minD* DNA, 0.25 μl of deoxyribonuclease (DNase) I (2 U μl^{-1}; NEB) was transferred into an empty PCR tube. Using a cut pipette tip, 7 μl of liposomes were transferred to the PCR tubes and mixed with the DNase I by pipetting up and down three times. Liposomes were incubated at 37°C for 3 to 16 hours in a thermocycler. The chambers (5.7 mm by 6.1 mm; length × width) of a μ-Slide 18 Well Glass Bottom (Ibidi) were preincubated with 50 μl of bovine serum albumin (BSA; 1 mg ml^{-1}) in Milli-Q water for 10 min and subsequently washed three times with Milli-Q water and once with PB buffer [20 mM Hepes-KOH (pH 7.6), 180 mM potassium glutamate, and 14 mM magnesium acetate]. Liposomes were diluted 50-fold in PB buffer of which 50 μl was transferred to each chamber. The imaging slide was kept overnight in the dark at 4°C to allow for the liposomes to sediment.

Downloaded from https://www.science.org at Delft University on June 17, 2026

For experiments with MinD and MinE, the liposome suspension obtained after swelling was diluted twofold using a mixture of 1:1 PURE*frex* 2.0 Solution I and Milli-Q water supplemented with 2.5 mM ATP and DNase I (0.13 U μl^{-1}). Next, 10 µl of the diluted liposome sample was transferred to an in-house made, BSA-functionalized round imaging chamber (diameter of ~3 mm). The sample slide was incubated in a laboratory incubator at 37°C for 2 to 3 hours before imaging at room temperature.

Confocal microscopy

Liposomes were imaged using the A1R Laser scanning confocal microscope (Nikon) equipped with an SR Apo TIRF 100× oil immersion objective (NA of 1.49). Imaging was performed using laser line of 488 nm with emission filter 525/50 nm [gallium arsenide phosphide (GaAsP) detector; YFP and eGFP-MinC], laser line of 561 nm with emission filter 595/50 nm (GaAsP detector; PAmCherry2), and laser line of 640 nm with emission filter 700/75 nm (photomultiplier tube detector; DOPE-Cy5). For image-based screening, channels 1 (YFP, eGFP-MinC) and 3 (DOPE-Cy5) were imaged simultaneously. Imaging was performed at a fixed dwell time (2.2 µs) and image size (512 × 512 pixels, 0.25 µm $pixel^{-1}$) to optimize for high imaging speed. The pinhole size was 42.1 µm (1 Airy unit for 405 nm). Point stimulation was performed using the 405-nm laser for 300 ms at 10 to 50% laser power (34 to 167 µW). Image acquisition and stimulation were operated by NIS-Elements version 5.30.07 (Nikon) at room temperature with the focus drift correction module Perfect Focus System (Nikon) enabled.

For optimal stimulation accuracy, point stimulation was performed in the center of the FOV using the Galvano scanner mirrors. The point stimulation accuracy was regularly checked by the green-to-red photoconvertion of mEos2 using a 3-µl droplet of 50 µM protein in PB buffer sandwiched between a glass slide and coverslip and 1% laser power (5 µW) for 300 ms (fig. S9). When a misalignment of a few pixels was observed, the stage position was adjusted accordingly. The absolute laser powers (in microwatt) for point stimulation were measured by a Microscope Slide Photodiode Power Sensor with 18 mm by 18 mm Active Area (S170C, THORLABS Germany) placed on top of the 100× objective (without oil) and connected to a Digital Optical Power and Energy Meter (PM100D, THORLABS Germany). The absolute power was measured for 1, 10, 25, and 50% relative laser powers while point stimulating in the center of the FOV. The power value was averaged over 10 s. Deviations from the above-mentioned protocols for some experiments are described in tables S1, S7, S10, and S11.

Quantification of the lumen intensities of target and off-target liposomes

To quantify the change of PAmCherry2 fluorescence intensity upon stimulation, liposomes expressing YFP were imaged before and 10 s after stimulation. Using Fiji (ImageJ2 v2.9.0) (*64*), the PAmCherry2 and YFP intensities were measured for the target liposome and all off-target liposomes within a distance of 15 µm. For each liposome, an area was defined manually that covered most of the lumen, of which the average intensity was calculated.

Training and testing of YOLO

Train and test sets for YOLOv3-tiny (*43*) and YOLOv7-tiny (*44*) algorithms were generated by manually drawing bounding boxes using the open-source software Label Studio (*65*) (https://github.com/heartexlabs/label-studio). While labeling, the individual imaging channels were also inspected using Fiji (ImageJ2 v2.9.0) (*64*). The YOLO models were trained and tested on GPU using a Google Colaboratory notebook (available at https://github.com/DanelonLab/Image-based-Phenotypic-Selection/tree/main/Training-YOLO), which was adapted from https://github.com/theAIGuysCode/YOLOv3-Cloud-Tutorial. Unless indicated otherwise, the training of YOLO algorithms was performed from scratch (i.e., without using pretrained weights) using jpg images of 512 × 512 pixels. During training, saturation and exposure (brightness) augmentations were enabled, but color and rotation augmentations were disabled. The random parameter was disabled to prevent up- and downscaling of images during training. For YOLO algorithms trained on 1 class (MinD localized on the membrane), a dataset was used consisting of 700 images containing 688 labeled instances. For YOLO algorithms trained on 2 classes, 40 images were used containing 1645 instances, 915 without membrane-localized eGFP-MinC (class 1), and 730 instances with membrane-localized eGFP-MinC (class 2). For the 2-class YOLO model (used for detection of dynamical behaviors), special care was taken to exclude (i) small liposomes (approximately <6 µm), which tend to move in and out of focus more frequently than larger liposomes; (ii) liposomes with a blurry, undefined membrane signal; and (iii) liposomes at the edges of the image. The YOLO models were trained and tested using 80 and 20% of the images, respectively. After validation of the two-class model, a new model was trained on 100% of the data and used for the experiments.

Real-time image analysis

Real-time image analysis was performed on a HP Z4 workstation with Intel(R) Xeon(R) W-2145 CPU, 64 GB ram, NVIDIA Quadro RTX 4000 GPU, and Windows 10 Enterprise operating system. To run YOLO, open-source software CUDA v10.2, cuDNN v8.0.2, OpenCV v4.2.0 and Darknet were installed. Darknet was downloaded from https://github.com/AlexeyAB/darknet and compiled using Visual Studio 2019 as described on https://github.com/AlexeyAB/darknet#requirements-for-windows-linux-and-macos.

Automated image acquisition, image analysis, and laser stimulation were controlled by the JOBS module of the NIS-Elements image acquisition software (Nikon). Real-time image analysis by intensity thresholding and simple morphology constraints was performed by the General Analysis module in NIS-Elements (JOB available at https://github.com/DanelonLab/Image-based-Phenotypic-Selection/tree/main/Detection-By-Intensity-Thresholding). This module applied general convolution (size: 3), intensity thresholding, and size (3.5 to 20 µm) and circularity (0.3 to 1) constraints to the YFP channel.

For object detection by YOLO, the OutProc function within JOBS exported the image to a local computer folder and initiated a Windows batch script which started YOLO and redirected the resulting coordinates back to NIS-Elements for stimulation (JOB and code available at https://github.com/DanelonLab/Image-based-Phenotypic-Selection/tree/main/Detection-By-YOLO-Single-Time-Frame).

For video-based classification, the liposomes detected in multiple time frames were identified as the same object based on the nearest neighbor with a maximum distance of 5 µm. Bounding boxes with an x-to-y ratio smaller than 0.7 or larger than 1.3 (these were typically liposomes at the edge of the FOV) and/or an area smaller than 37 μm^2 were excluded from the analysis. Liposomes whose

Downloaded from https://www.science.org at Delft University on June 17, 2026

classes changed across the different time frames were classified as dynamic and their coordinates were imported by NIS-Elements for stimulation. The JOB and code for video-based classification are available at https://github.com/DanelonLab/Image-based-Phenotypic-Selection/tree/main/Detection-By-YOLO-Using-Videos. ChatGPT was used to assist in generating parts of the Windows batch scripts.

Flow cytometry

Liposomes were transferred from the imaging chamber to an Eppendorf tube using a cut pipette tip. The imaging chambers were washed two times with 50 µl of PB buffer, and this volume was added to the same Eppendorf tube. The sample was filtered using the 35-µm nylon mesh of a cell strainer cap of 5-ml round bottom polystyrene test tubes (Falcon). Liposomes were screened and sorted with the BD FACSMelody cell sorter (BD Biosciences) using a 100-µm nozzle, laser line of 488 nm with emission filter 527/32 nm (YFP, eGFP-MinC), and laser line of 561 nm with emission filter 582/15 nm (PAmCherry2). The photomultiplier tube voltages were set at 342 V for FSC, 405 V for SSC (with SSC threshold 359 V), 646 V for YFP and eGFP-MinC, and 660 V for PAmCherry2. Data were processed with BD FACSChorus version 3 (while sorting) or Cytobank (https://community.cytobank.org/) as shown in fig. S10. The liposomes sorted by FACS were heated at 75°C for 15 min to inactivate DNase I.

Quantitative PCR

Quantitative PCR reactions contained 1× PowerUP SYBR Green Master Mix (Applied Biosystems), 400 nM each primer (1121 ChD and 1122 ChD for *YFP*, 1208 ChD and 1209 ChD for *minD*, and 1414 ChD and 1415 ChD for *btubB*) and 1 µl of heat-inactivated liposome sample in a total volume of 10 µl. Quantitative PCR reactions were performed using the Quantstudio 5 Real-Time PCR system (Thermo Fisher Scientific). The samples were incubated sequentially for 2 min at 50°C, 5 min at 94°C, 45 cycles of 15 s at 94°C, 15 s at 56°C, 30 s at 68°C, followed by 5 min at 68°C and a melting curve from 65° to 95°C. The DNA concentration was calculated using calibration curves ranging from 0.00001 to 100 pM in the Quantstudio Design and Analysis software v1.4.3 (Thermo Fisher Scientific).

DNA recovery from liposomes and Nanopore sequencing

DNA (*minD*) was recovered from liposomes by PCR. The reactions were set up at 50-µl volume and contained 400 µM dNTPs, 300 nM each primer (1525/1526 ChD), 0.4 U of KOD Xtreme Hot Start DNA Polymerase and 2 µl of heat-inactivated liposome sample in 1× KOD Xtreme PCR Buffer. The thermocycling reaction was performed as follows: 94°C for 2 min, (98°C for 10 s, 56°C for 30 s, 68°C for 84 s) × 39. The amplicons were purified with the QIAquick PCR Cleanup Kit (QIAGEN). The recovery of the DNA [1398 base pairs (bp)] from liposomes was verified using gel electrophoresis, and the DNA concentration was measured by the NanoDrop 2000c spectrophotometer (Isogen Life Science). Nanopore sequencing was performed by Plasmidsaurus. Using the Galaxy web platform (*66*) (https://usegalaxy.org), the raw sequencing reads were filtered based on size (1100 to 1400 bp) and mapped to the reference sequence using the Filter FASTQ reads by quality score and length (*67*) and Map with minimap2 (*68*) tools, respectively, using default parameters. The mapped reads were further processed with in-house written R scripts run in Rstudio (R v4.4.1) (https://github.com/DanelonLab/MOSAIC/tree/main/Application-MinD-MTS-Library). The DNA sequences encoding the MTS of MinD were extracted from the mapped reads and subjected to a quality control, whereafter the different DNA variants among those sequences were counted.

Statistical analysis

Error bars in bar plots indicate the SD. The box-whisker plots in Fig. 2A and fig. S1 display the median (middle line), the 75/25 percentiles at the boxes and the 90/10 at the whiskers. Statistical tests in fig. S1 (Mann-Whitney tests, correlation analysis, linear regression, unpaired *t* tests) were performed using GraphPad Prism v10.0.3 and were significant if P value (two-tailed) < 0.05. Pearson's r is the Pearson correlation coefficient. R^2 is the coefficient of determination. The number of biological replicates (i.e., distinct liposome samples) and technical replicates (repeated measurements) are indicated in the figure legends. The brightness and contrast of microscopy images were adjusted identically for multiple images when comparing fluorescence intensities using Fiji (ImageJ2 v2.9.0) (*64*).

Supplementary Materials

The PDF file includes:

Figs. S1 to S10
Tables S1 to S14
DNA sequences
Legend for data S1

Other Supplementary Material for this manuscript includes the following:

Data S1

REFERENCES

1. P. van Nies, I. Westerlaken, D. Blanken, M. Salas, M. Mencía, C. Danelon, Self-replication of DNA by its encoded proteins in liposome-based synthetic cells. *Nat. Commun.* **9**, 1583 (2018).
2. S. M. Nomura, K. Tsumoto, T. Hamada, K. Akiyoshi, Y. Nakatani, K. Yoshikawa, Gene expression within cell-sized lipid vesicles. *Chembiochem* **4**, 1172–1175 (2003).
3. V. Noireaux, A. Libchaber, A vesicle bioreactor as a step toward an artificial cell assembly. *Proc. Natl. Acad. Sci. U.S.A.* **101**, 17669–17674 (2004).
4. H. Saito, Y. Kato, M. Le Berre, A. Yamada, T. Inoue, K. Yosikawa, D. Baigl, Time-resolved tracking of a minimum gene expression system reconstituted in giant liposomes. *Chembiochem* **10**, 1640–1643 (2009).
5. A. Scott, M. J. Noga, P. de Graaf, I. Westerlaken, E. Yildirim, C. Danelon, Cell-free phospholipid biosynthesis by gene-encoded enzymes reconstituted in liposomes. *PLOS ONE* **11**, e0163058 (2016).
6. D. Blanken, D. Foschepoth, A. C. Serrão, C. Danelon, Genetically controlled membrane synthesis in liposomes. *Nat. Commun.* **11**, 4317 (2020).
7. S. Eto, R. Matsumura, Y. Shimane, M. Fujimi, S. Berhanu, T. Kasama, Y. Kuruma, Phospholipid synthesis inside phospholipid membrane vesicles. *Commun. Biol.* **5**, 1–11 (2022).
8. A. Bhattacharya, R. J. Brea, H. Niederholtmeyer, N. K. Devaraj, A minimal biochemical route towards de novo formation of synthetic phospholipid membranes. *Nat. Commun.* **10**, 300 (2019).
9. T. Furusato, F. Horie, H. T. Matsubayashi, K. Amikura, Y. Kuruma, T. Ueda, De novo synthesis of basal bacterial cell division proteins FtsZ, FtsA, and ZipA inside giant vesicles. *ACS Synth. Biol.* **7**, 953–961 (2018).
10. E. Godino, J. N. López, D. Foschepoth, C. Cleij, A. Doerr, C. F. Castellà, C. Danelon, De novo synthesized Min proteins drive oscillatory liposome deformation and regulate FtsA-FtsZ cytoskeletal patterns. *Nat. Commun.* **10**, 4969 (2019).
11. E. Godino, J. N. López, I. Zarguit, A. Doerr, M. Jimenez, G. Rivas, C. Danelon, Cell-free biogenesis of bacterial division proto-rings that can constrict liposomes. *Commun. Biol.* **3**, 539 (2020).
12. J. Kattan, A. Doerr, M. Dogterom, C. Danelon, Shaping liposomes by cell-free expressed bacterial microtubules. *ACS Synth. Biol.* **10**, 2447–2455 (2021).
13. S. Kohyama, A. Merino-Salomón, P. Schwille, In vitro assembly, positioning and contraction of a division ring in minimal cells. *Nat. Commun.* **13**, 6098 (2022).
14. N. De Franceschi, R. Barth, S. Meindlhumer, A. Fragasso, C. Dekker, Dynamin A as a one-component division machinery for synthetic cells. *Nat. Nanotechnol.* **19**, 70–76 (2024).

Downloaded from https://www.science.org at Delft University on June 17, 2026

15. E. Godino, A. M. Restrepo Sierra, C. Danelon, Imaging flow cytometry for high-throughput phenotyping of synthetic cells. *ACS Synth. Biol.* **12**, 2015–2028 (2023).
16. Z. Abil, C. Danelon, Roadmap to building a cell: An evolutionary approach. *Front. Bioeng. Biotechnol.* **8**, 927 (2020).
17. M. S. Packer, D. R. Liu, Methods for the directed evolution of proteins. *Nat. Rev. Genet.* **16**, 379–394 (2015).
18. Z. Abil, A. M. Restrepo Sierra, A. R. Stan, A. Chân, A. del Prado, M. de Vega, Y. Rondelez, C. Danelon, Darwinian evolution of self-replicating DNA in a synthetic protocell. *Nat. Commun.* **15**, 9091 (2024).
19. S. Fujii, T. Matsuura, T. Sunami, T. Nishikawa, Y. Kazuta, T. Yomo, Liposome display for in vitro selection and evolution of membrane proteins. *Nat. Protoc.* **9**, 1578–1591 (2014).
20. T. Sunami, K. Sato, T. Matsuura, K. Tsukada, I. Urabe, T. Yomo, Femtoliter compartment in liposomes for in vitro selection of proteins. *Anal. Biochem.* **357**, 128–136 (2006).
21. T. Nishikawa, T. Sunami, T. Matsuura, N. Ichihashi, T. Yomo, Construction of a gene screening system using giant unilamellar liposomes and a fluorescence-activated cell sorter. *Anal. Chem.* **84**, 5017–5024 (2012).
22. S. Fujii, T. Matsuura, T. Sunami, Y. Kazuta, T. Yomo, In vitro evolution of α-hemolysin using a liposome display. *Proc. Natl. Acad. Sci. U.S.A.* **110**, 16796–16801 (2013).
23. A. Uyeda, T. Watanabe, Y. Kato, H. Watanabe, T. Yomo, T. Hohsaka, T. Matsuura, Liposome-based in vitro evolution of aminoacyl-tRNA synthetase for enhanced pyrrolysine derivative incorporation. *Chembiochem* **16**, 1797–1802 (2015).
24. A. Uyeda, S. Nakayama, Y. Kato, H. Watanabe, T. Matsuura, Construction of an in vitro gene screening system of the E. coli EmrE transporter using liposome display. *Anal. Chem.* **88**, 12028–12035 (2016).
25. Y. Murase, H. Nakanishi, G. Tsuji, T. Sunami, N. Ichihashi, In vitro evolution of unmodified 16S rRNA for simple ribosome reconstitution. *ACS Synth. Biol.* **7**, 576–583 (2018).
26. R. T. Walton, A. Singh, P. C. Blainey, Pooled genetic screens with image-based profiling. *Mol. Syst. Biol.* **18**, e10768 (2022).
27. D. Schraivogel, T. M. Kuhn, B. Rauscher, M. Rodríguez-Martínez, M. Paulsen, K. Owsley, A. Middlebrook, C. Tischer, B. Ramasz, D. Ordoñez-Rueda, M. Dees, S. Cuylen-Haering, E. Diebold, L. M. Steinmetz, High-speed fluorescence image–enabled cell sorting. *Science* **375**, 315–320 (2022).
28. M. S. Paulsen, "Image-enabled cell sorting using the BD CellView Technology" in *Flow Cytometry Protocols*, T. S. Hawley, R. G. Hawley, Eds. (Springer US, New York, NY, 2024), pp. 145–158.
29. A. Isozaki, H. Mikami, H. Tezuka, H. Matsumura, K. Huang, M. Akamine, K. Hiramatsu, T. Iino, T. Ito, H. Karakawa, Y. Kasai, Y. Li, Y. Nakagawa, S. Ohnuki, T. Ota, Y. Qian, S. Sakuma, T. Sekiya, Y. Shirasaki, N. Suzuki, E. Tayyabi, T. Wakamiya, M. Xu, M. Yamagishi, H. Yan, Q. Yu, S. Yan, D. Yuan, W. Zhang, Y. Zhao, F. Arai, R. E. Campbell, C. Danelon, D. D. Carlo, K. Hiraki, Y. Hoshino, Y. Hosokawa, M. Inaba, A. Nakagawa, Y. Ohya, M. Oikawa, S. Uemura, Y. Ozeki, T. Sugimura, N. Nitta, K. Goda, Intelligent image-activated cell sorting 2.0. *Lab Chip* **20**, 2263–2273 (2020).
30. T. M. Kuhn, M. Paulsen, S. Cuylen-Haering, Accessible high-speed image-activated cell sorting. *Trends Cell Biol.* **34**, 657–670 (2024).
31. N. S. Barteneva, E. Fasler-Kan, I. A. Vorobjev, Imaging flow cytometry: Coping with heterogeneity in biological systems. *J. Histochem. Cytochem.* **60**, 723–733 (2012).
32. N. Hasle, A. Cooke, S. Srivatsan, H. Huang, J. J. Stephany, Z. Krieger, D. Jackson, W. Tang, S. Pendyala, R. J. Monnat Jr., C. Trapnell, E. M. Hatch, D. M. Fowler, High-throughput, microscope-based sorting to dissect cellular heterogeneity. *Mol. Syst. Biol.* **16**, e9442 (2020).
33. J. Lee, Z. Liu, P. H. Suzuki, J. F. Ahrens, S. Lai, X. Lu, S. Guan, F. St-Pierre, Versatile phenotype-activated cell sorting. *Sci. Adv.* **6**, eabb7438 (2020).
34. X. Yan, N. Stuurman, S. A. Ribeiro, M. E. Tanenbaum, M. A. Horlbeck, C. R. Liem, M. Jost, J. S. Weissman, R. D. Vale, High-content imaging-based pooled CRISPR screens in mammalian cells. *J. Cell Biol.* **220**, e202008158 (2021).
35. G. Kanfer, S. A. Sarraf, Y. Maman, H. Baldwin, E. Dominguez-Martin, K. R. Johnson, M. E. Ward, M. Kampmann, J. Lippincott-Schwartz, R. J. Youle, Image-based pooled whole-genome CRISPRi screening for subcellular phenotypes. *J. Cell Biol.* **220**, e202006180 (2021).
36. L. You, P.-R. Su, M. Betjes, R. G. Rad, T.-C. Chou, C. Beerens, E. van Oosten, F. Leufkens, P. Gasecka, M. Muraro, R. van Tol, D. van Steenderen, S. Farooq, J. A. U. Hardillo, R. B. de Jong, D. Brinks, M.-P. Chien, Linking the genotypes and phenotypes of cancer cells in heterogenous populations via real-time optical tagging and image analysis. *Nat. Biomed. Eng.* **6**, 667–675 (2022).
37. H. Tian, H. C. Davis, J. D. Wong-Campos, P. Park, L. Z. Fan, B. Gmeiner, S. Begum, C. A. Werley, G. B. Borja, H. Upadhyay, H. Shah, J. Jacques, Y. Qi, V. Parot, K. Deisseroth, A. E. Cohen, Video-based pooled screening yields improved far-red genetically encoded voltage indicators. *Nat. Methods* **20**, 1082–1094 (2023).
38. C. Lin, L. Liu, P. Zou, Functional imaging-guided cell selection for evolving genetically encoded fluorescent indicators. *Cell Rep. Methods* **3**, 100544 (2023).
39. Y. Shimizu, A. Inoue, Y. Tomari, T. Suzuki, T. Yokogawa, K. Nishikawa, T. Ueda, Cell-free translation reconstituted with purified components. *Nat. Biotechnol.* **19**, 751–755 (2001).
40. E. Moen, D. Bannon, T. Kudo, W. Graf, M. Covert, D. Van Valen, Deep learning for cellular image analysis. *Nat. Methods* **16**, 1233–1246 (2019).
41. B. Chai, C. Efstathiou, H. Yue, V. M. Draviam, Opportunities and challenges for deep learning in cell dynamics research. *Trends Cell Biol.* **34**, 955–967 (2024).
42. J. Redmon, S. Divvala, R. Girshick, A. Farhadi, You Only Look Once: Unified, real-time object detection. arXiv:1506.02640 [cs.CV] (2016).
43. J. Redmon, A. Farhadi, YOLOv3: An incremental improvement. arXiv: 1804.02767 [cs.CV] (2018).
44. C.-Y. Wang, A. Bochkovskiy, H.-Y. M. Liao, YOLOv7: Trainable bag-of-freebies sets new state-of-the-art for real-time object detectors. arXiv: 2207.02696 [cs.CV] (2022).
45. T. Litschel, B. Ramm, R. Maas, M. Heymann, P. Schwille, Beating vesicles: Encapsulated protein oscillations cause dynamic membrane deformations. *Angew. Chem. Int. Ed. Engl.* **57**, 16286–16290 (2018).
46. V. W. Rowlett, W. Margolin, The Min system and other nucleoid-independent regulators of Z ring positioning. *Front. Microbiol.* **6**, 478 (2015).
47. T. H. Szeto, S. L. Rowland, L. I. Rothfield, G. F. King, Membrane localization of MinD is mediated by a C-terminal motif that is conserved across eubacteria, archaea, and chloroplasts. *Proc. Natl. Acad. Sci. U.S.A.* **99**, 15693–15698 (2002).
48. K. Seo, K. Hagino, N. Ichihashi, "Progresses in cell-free in vitro evolution" in *Cell-Free Production: System Development*, Y. Lu, M. C. Jewett, Eds. (Springer Nature Switzerland, 2023), pp. 121–140.
49. Z. Abil, A. M. Restrepo Sierra, C. Danelon, Clonal amplification-enhanced gene expression in synthetic vesicles. *ACS Synth. Biol.* **12**, 1187–1203 (2023).
50. K. K. Yang, Z. Wu, F. H. Arnold, Machine-learning-guided directed evolution for protein engineering. *Nat. Methods* **16**, 687–694 (2019).
51. A. Pandi, C. Diehl, A. Yazdizadeh Kharrazi, S. A. Scholz, E. Bobkova, L. Faure, M. Nattermann, D. Adam, N. Chapin, Y. Foroughijabbari, C. Moritz, N. Paczia, N. S. Cortina, J.-L. Faulon, T. J. Erb, A versatile active learning workflow for optimization of genetic and metabolic networks. *Nat. Commun.* **13**, 3876 (2022).
52. D. Blanken, P. van Nies, C. Danelon, Quantitative imaging of gene-expressing liposomes reveals rare favorable phenotypes. *Phys. Biol.* **16**, 045002 (2019).
53. C. A. Werley, M.-P. Chien, A. E. Cohen, Ultrawidefield microscope for high-speed fluorescence imaging and targeted optogenetic stimulation. *Biomed. Opt. Express* **8**, 5794–5813 (2017).
54. N. Peterman, E. Levine, Sort-seq under the hood: Implications of design choices on large-scale characterization of sequence-function relations. *BMC Genomics* **17**, 206 (2016).
55. Z. Nourian, W. Roelofsen, C. Danelon, Triggered gene expression in fed-vesicle microreactors with a multifunctional membrane. *Angew. Chem. Int. Ed. Engl.* **51**, 3114–3118 (2012).
56. L. Van de Cauter, F. Fanalista, L. van Buren, N. De Franceschi, E. Godino, S. Bouw, C. Danelon, C. Dekker, G. H. Koenderink, K. A. Ganzinger, Optimized cDICE for efficient reconstitution of biological systems in giant unilamellar vesicles. *ACS Synth. Biol.* **10**, 1690–1702 (2021).
57. D. T. Gonzales, N. Yandrapalli, T. Robinson, C. Zechner, T.-Y. D. Tang, Cell-free gene expression dynamics in synthetic cell populations. *ACS Synth. Biol.* **11**, 205–215 (2022).
58. P.-R. Su, L. You, C. Beerens, K. Bezstarosti, J. Demmers, M. Pabst, R. Kanaar, C.-C. Hsu, M.-P. Chien, Microscopy-based single-cell proteomic profiling reveals heterogeneity in DNA damage response dynamics. *Cell Rep. Methods* **2**, 100237 (2022).
59. H. M. Bennett, W. Stephenson, C. M. Rose, S. Darmanis, Single-cell proteomics enabled by next-generation sequencing or mass spectrometry. *Nat. Methods* **20**, 363–374 (2023).
60. A. Pratapa, M. Doron, J. C. Caicedo, Image-based cell phenotyping with deep learning. *Curr. Opin. Chem. Biol.* **65**, 9–17 (2021).
61. L. Olivi, C. Bagchus, V. Pool, E. Bekkering, K. Speckner, H. Offerhaus, W. Y. Wu, M. Depken, K. J. A. Martens, R. H. J. Staals, J. Hohlbein, Live-cell imaging reveals the trade-off between target search flexibility and efficiency for Cas9 and Cas12a. *Nucleic Acids Res.* **52**, 5241–5256 (2024).
62. M. Loose, E. Fischer-Friedrich, C. Herold, K. Kruse, P. Schwille, Min protein patterns emerge from rapid rebinding and membrane interaction of MinE. *Nat. Struct. Mol. Biol.* **18**, 577–583 (2011).
63. P. Galka, E. Jamez, G. Joachim, P. Soumillion, QuickLib, a method for building fully synthetic plasmid libraries by seamless cloning of degenerate oligonucleotides. *PLOS ONE* **12**, e0175146 (2017).
64. J. Schindelin, I. Arganda-Carreras, E. Frise, V. Kaynig, M. Longair, T. Pietzsch, S. Preibisch, C. Rueden, S. Saalfeld, B. Schmid, J.-Y. Tinevez, D. J. White, V. Hartenstein, K. Eliceiri, P. Tomancak, A. Cardona, Fiji: An open-source platform for biological-image analysis. *Nat. Methods* **9**, 676–682 (2012).
65. M. Tkachenko, M. Malyuk, A. Holmanyuk, N. Liubimov, Label Studio: Data labeling software, (2020); https://github.com/HumanSignal/label-studio.
66. The Galaxy Community, The Galaxy platform for accessible, reproducible and collaborative biomedical analyses: 2022 update. *Nucleic Acids Res.* **50**, W345–W351 (2022).

Downloaded from https://www.science.org at Delft University on June 17, 2026

67. D. Blankenberg, A. Gordon, G. Von Kuster, N. Coraor, J. Taylor, A. Nekrutenko Galaxy Team, Manipulation of FASTQ data with Galaxy. *Bioinformatics* **26**, 1783–1785 (2010).
68. H. Li, Minimap2: Pairwise alignment for nucleotide sequences. *Bioinformatics* **34**, 3094–3100 (2018).

Acknowledgments: *PAmCherry2.1* gene was a gift from the Van der Oost group (Wageningen University, the Netherlands). G571 (pRSET-mEos2) was a gift from K. Grüßmayer (TU Delft, the Netherlands). We thank I. Westerlaken for the purification of PAmCherry2 and mEos2. We thank R. Knot for preliminary experimental work and M. van Tongeren for performing preliminary tests with YOLO. We are also thankful to M. Shemesh, M. Holub, T. Kuijt (Nikon Instruments), and the technical support team from Laboratory Imaging s.r.o. for the help with the microscopy automation; T. Langlois and D. Loras from BD Life Sciences–Biosciences for fruitful discussions and testing the BD FACSDiscover S8; and M.-P. Chien and the Chien laboratory for testing their ultrawide-FOV microscope with our liposome samples. We are grateful to GeneFrontier for sponsoring our research. **Funding:** M.v.d.B., C.D., M.S., and N.J.C. acknowledge financial support from the "BaSyC – Building a Synthetic Cell" Gravitation grant (024.003.019) of the Netherlands Ministry of Education, Culture and Science (OCW) and the Netherlands Organisation for Scientific Research (NWO). C.D. acknowledges funding from Agence Nationale de la Recherche (ANR-22-CPJ2–0091-01). N.J.C. acknowledges funding by the NWO-SUMMIT grant "Evolving life from non-life (EVOLF)" (SUMMIT.1.004). **Author contributions:** Conceptualization: C.D. and M.v.d.B. Methodology: C.D., M.v.d.B., and M.S. Investigation: M.v.d.B. and M.S. Formal analysis: M.v.d.B. Validation: C.D. and M.v.d.B. Software: M.v.d.B. Visualization: M.v.d.B. Resources: C.D. Data curation: M.v.d.B and C.D. Supervision: C.D. and N.J.C. Writing—original draft: M.v.d.B. and C.D. Writing—review and editing: C.D., N.J.C., and M.v.d.B. Project administration: C.D. Funding acquisition: C.D. and N.J.C. **Competing interests:** The authors declare that they have no competing interest. **Data, code, and materials availability:** All data and code needed to evaluate and reproduce the results in the paper are present in the paper, the Supplementary Materials, and/or data S1 (benchmarking overview). Supplementary Materials include confocal fluorescence images, FACS plots, qPCR data, performance of object detection models, agarose gel electrophoresis, lists of primers and plasmids, tables with experimental details, and DNA sequences. Raw and processed data underlying this article are available in the 4TU.ResearchData repository with DOI: 10.4121/60cdce27-5bd5-44ec-9d8f-53f2ef6b9d58. The codes used in this article are available in the 4TU.ResearchData repository with DOI: 10.4121/60cdce27-5bd5-44ec-9d8f-53f2ef6b9d58 and on GitHub at https://github.com/DanelonLab/Image-based-Phenotypic-Selection under the MIT license and archived on Zenodo with DOI: 10.5281/zenodo.18925370. Materials such as plasmids and primers constructed for this study are available from the authors upon request (danelon@insa-toulouse.fr).

Submitted 16 October 2025
Accepted 27 April 2026
Published 3 June 2026
10.1126/sciadv.aed0860

Downloaded from https://www.science.org at Delft University on June 17, 2026

ScienceAdvances

Image-based phenotypic sorting of synthetic cells

Marijn van den Brink, Marlena Stam, Nico J. Claassens, and Christophe Danelon

Sci. Adv. **12** (23), eaed0860. DOI: 10.1126/sciadv.aed0860

View the article online
https://www.science.org/doi/10.1126/sciadv.aed0860
Permissions
https://www.science.org/help/reprints-and-permissions

Downloaded from https://www.science.org at Delft University on June 17, 2026

Use of this article is subject to the Terms of service

Science Advances (ISSN 2375-2548) is published by the American Association for the Advancement of Science. 1200 New York Avenue NW, Washington, DC 20005. The title *Science Advances* is a registered trademark of AAAS.

Copyright © 2026 The Authors, some rights reserved; exclusive licensee American Association for the Advancement of Science. No claim to original U.S. Government Works. Distributed under a Creative Commons Attribution License 4.0 (CC BY).